Journal of Low Temperature Physics (2020) 199:275–280
https://doi.org/10.1007/s10909-020-02342-4

A Predictive Control Algorithm for Time-Division-Multiplexed Readout of TES Microcalorimeters

Malcolm Durkin[1] · G. C. O'Neil[2] · W. B. Doriese[2] · J. D. Gard[1,2] · G. C. Hilton[2] · J. Imrek[1,2] · N. Ortiz[1,2] · C. D. Reintsema[2] · R. W. Stevens[1,2] · D. S. Swetz[2] · J. N. Ullom[1,2]

Received: 18 August 2019 / Accepted: 13 January 2020 / Published online: 28 January 2020

Abstract
Time division multiplexing (TDM) uses a digital flux-locked loop (DFLL) to linearize each first-stage SQUID amplifier. Presently, the dynamic range of our TDM systems is limited by the use of a proportional-integral controller to maintain the DFLL. In this paper, we use simulations to assess the improvements possible with a predictive control algorithm that anticipates rapid changes in transition-edge sensor current during the rising edge of an X-ray pulse. We calculate that the predictive control algorithm can improve our TDM architecture's dynamic range by 35%. This significant increase in multiplexing capabilities could be used to read out higher-energy X-rays, reduce readout noise, increase multiplexing factors, or reduce SQUID power output.

Keywords Transition-edge sensor · Multiplexing · Microcalorimeter

1 Introduction

Time division multiplexing (TDM) is the most mature readout technology for transition-edge sensor (TES) X-ray microcalorimeters. TDM systems of the scale of 250 pixels have been deployed in a broad range of terrestrial X-ray applications [1], including recently at an electron-beam ion-trap (EBIT) facility [2] and in exotic-atom experiments [3, 4]. TDM is being developed as the backup readout technology for the Athena X-ray satellite mission [5]. A recent demonstration [6] has shown that TDM can meet the requirements of the Athena X-ray Integral Field Unit (X-IFU)

✉ Malcolm Durkin
malcolm.durkin@nist.gov

1 University of Colorado, Boulder, CO, USA

2 National Institute of Standards and Technology, Boulder, CO, USA

instrument [7], but spacecraft resources like power and weight are so precious that further improvements to the multiplexing factor, noise, and SQUID power consumption are highly desirable. In this paper, we investigate the increase in superconducting quantum interference device (SQUID) dynamic range offered by an improved digital flux-locked loop (DFLL) control algorithm.

TDM involves the sequential readout of TESs. In our architecture [8], each TES's current (I_{TES}) is read out as the flux input (Φ_{in}) to a first-stage SQUID amplifier (SQ1). The SQ1s are operated in rows and columns, where rows of SQ1s are read out in sequence and columns of SQ1s are read out in parallel. The SQ1s in a column share a flux-feedback line (FB1), and their current signals feed into a common SQUID series array amplifier (SSAA). Rows of SQ1s are activated one at a time, resulting in one TES being read out at a time per column. A readout cycle in which all rows are accessed is called a *frame*. We routinely use 8-column × 32-row TDM readout in fielded X-ray spectrometers. A recent set of experiments [6] showed the viability of 40-row TDM for the detector speed, energy resolution, and X-ray energies required by X-IFU. With presently implemented feedback algorithms and SQUID designs, X-IFU's stringent readout requirements would be difficult to achieve for TDM factors much beyond 40 rows.

TDM readout uses a digital flux-locked loop (DFLL), applying a different feedback current (I_{FB1}) during each row activation to attempt to keep the total flux (Φ) in each active SQ1 constant. In our existing system, the DFLL is maintained using a proportional-integral (PI) controller [9]. Each row has its own value of applied feedback flux (Φ_{FB1}), which is updated once per frame using the SSAA voltage for that row as an error signal (V_{err}) for the PI controller. TDM conditions do not favor the use of the proportional term, which is ineffective as the primary corrective term because V_{err} has nonmonotonic flux dependence, and we will omit it from further discussion. Thus, our control algorithm can be written as a recurrence relation

$$\Phi_{\mathrm{FB1},n+1} = \Phi_{\mathrm{FB1},n} + K_{\mathrm{I}}(V_{\mathrm{err},n} - V_{\mathrm{err0}}) \tag{1}$$

where n is the frame index and K_{I} is the integral coefficient of the controller. The sign of K_{I} determines whether the algorithm is locked on the positive or negative slope of the SQUID curve, and V_{err0} determines the V_{err} value that the SQ1 is locked to. (We express V_{err0} as the percentage of the V_{err} amplitude from the bottom of the SQ1 curve.) A significant flux offset from the lock point occurs when Φ_{in} is changing rapidly. To account for this flux error, the measured Φ_{in} is a linear combination of Φ_{FB1} and V_{err} given by

$$\Phi_{\mathrm{measured},n} = \Phi_{\mathrm{FB1},n} + K_{\mathrm{mix}}\,(V_{\mathrm{err},n} - V_{\mathrm{err0}}) \tag{2}$$

where K_{mix} is the negative reciprocal of the slope of the V_{err} versus Φ_{FB1} curve at the lock point and is used to estimate the flux offset based on measured V_{err}.

Most estimates of the maximum flux-slew rate allowed by TDM and related architectures assume there will be an unacceptable error in readout if the control algorithm cannot remain on a linear slope of the V_{err} versus Φ_{FB1} curve [5, 6, 10], because our Φ_{measured} extraction algorithm assumes linearity. To test this assumption, we performed 1-column × 32-row TDM readout of NASA-Goddard TES microcalorimeters [11, 12] receiving X-rays from a fluoresced Mn target. To reduce measurement time, the array was illuminated at a rate of 9.5 counts per second (cps) per pixel. We used 224 ns row times and 7.168 ms (1000 frame) record lengths. Holding the other parameters constant, V_{err0} was adjusted so the SQUID amplifiers would be in varying degrees of nonlinearity during the highest-slew rate segments of the pulse, with V_{err} for typical pulses shown in Fig. 1 (Left). Each lock point's data set was then analyzed separately using typical pulse processing techniques [13], including arrival time correction, with the best-fit energy resolutions shown in Fig. 1 (Right). Large degradation in energy resolution occurs when the controller becomes trapped on the opposite slope of the SQUID curve, which occurs at $V_{\mathrm{err0}}=41\%$ in our measurement. A faster converging controller would avoid this failure mode.

2 Predictive Control Algorithms

We explore the utility of a predictive control algorithm that uses a first-order extrapolation of the control signal [14] to anticipate changes in I_{TES} that will occur by the next frame. This first-order time delay correction is advantageous because it results in $(V_{\mathrm{err}}-V_{\mathrm{err0}})$ proportional to $\mathrm{d}^2I_{\mathrm{TES}}/\mathrm{d}t^2$, as opposed to $\mathrm{d}I_{\mathrm{TES}}/\mathrm{d}t$ as in the PI controller, meaning that the algorithm will typically have a lower error than the PI controller and that its error will converge to zero for a fixed slope. The predictive controller is implemented as follows:

$$\Phi_{\mathrm{FB1},n+1} = \Phi_{\mathrm{FB1},n} + K_{\mathrm{I}}\,(V_{\mathrm{err},n} - V_{\mathrm{err0}}) + d\Phi_{\mathrm{FB1},n} \tag{3}$$

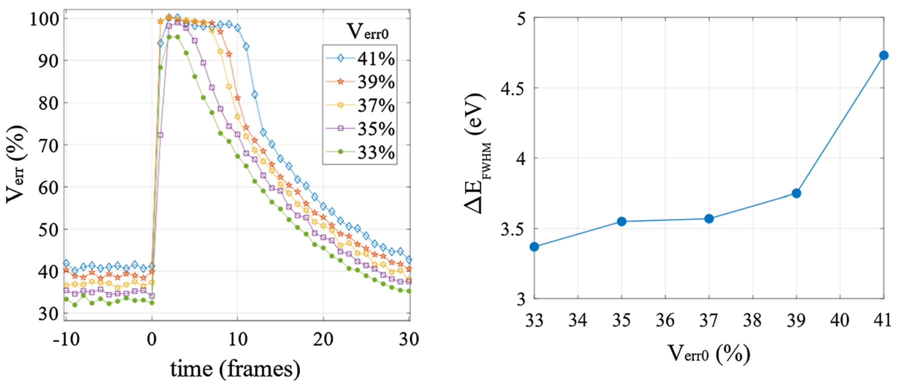

Fig. 1 (Left) The error signal for the rising edge of a typical Mn Kα pulse at various values of V_{err0}. As V_{err0} is increased, the V_{err} is increasingly distorted as it is moved farther into the nonlinear regime. For $V_{\mathrm{err}}>41\%$, SQ1s begin to unlock. (Right) The best fit resolution of the Mn Kα lines taken at 9.5 cps per pixel as V_{err0} is increased. Resolution degradation is initially gradual, but rapidly deteriorates at 41%. This failure corresponds to the controller being trapped in a region of nonlinearity for much of a pulse's rising edge (Color figure online)

where $d\Phi_{FB1}$ is the time delay correction term and is used to make a first-order correction to Φ_{FB1} based on its previous values. $d\Phi_{FB1}$ is not equivalent to a derivative term in a PID controller and is given by

$$d\Phi_{FB1,n} = (4\ d\Phi_{FB1,n-1} + \Phi_{FB1,n} - \Phi_{FB1,n-1})/5 \tag{4}$$

A numerical derivative of Φ_{FB1} with a lowpass first-order Butterworth filter is applied to improve stability.

A key failing of this predictive controller is that it is not well optimized to handle rapid changes in dI_{TES}/dt, such as those at the start of a pulse. This can be remedied by adding a rapid change to $d\Phi_{FB1}$ when the error exceeds a certain threshold. This time delay correction term is given by

$$d\Phi'_{FB1,n} = d\Phi'_{FB1,n} + K_{boost}\ K_{mix}\ (V_{err,n} - V_{err0}) \tag{5}$$

where K_{boost} tunes the adjustment. (K_{mix} is included so that $K_{boost}=1$ for a perfectly linear V_{err} function but should be set to greater values to account for nonlinearity.) To avoid instability, Eq. (5) is only applied once per rising edge of a pulse, accomplished by requiring 30 frames to pass before it can be applied again.

3 Simulations

We perform simulations to compare the performance of predictive controllers with (PC2) and without (PC1) using Eq. (5) to that of a PI controller. The input signal is given by a parabolic approximation of the rising edge of an X-ray pulse, shown in Fig. 2 (Left); this is sent into an asymmetric SQUID readout curve, shown in Fig. 2 (Center) with the result used as the error signal of the control function. Signal readout is performed by locking the controller at $V_{err0}=50\%$ on the steep slope and

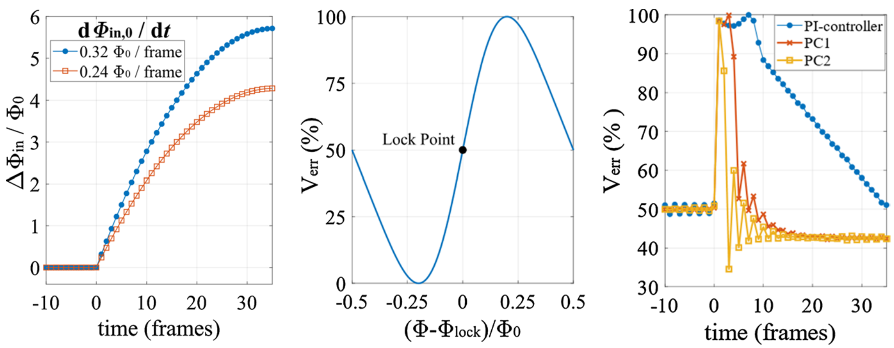

Fig. 2 (Left) Two examples of the TES pulse rising edge used in our simulations plotted as flux input to SQ1 versus time after X-ray arrival. Each pulse's flux-slew rate is at maximum value ($d\Phi_{in,0}/dt$) at the start of the pulse and linearly decreases in time to zero at 35 frames. (Center) The SQUID transfer function used in the simulations. The shape assumes a small amount of self-feedback to SQ1 and a perfectly linear SSAA. (Right) The error signal of the three algorithms tested using a pulse with $d\Phi_{in,0}/dt=0.24\ \Phi_0$/frame (Color figure online)

entering feedback and error signals into Eq. (2) to obtain measured flux. The controller parameter K_I is set to be as large as possible without the controller becoming unstable.

We initially study the algorithms in the most difficult pulse arrival scenario, when the pulse arrives at the same time as a data sampling (a pulse-sampling phase offset of zero) and $(\Phi - \Phi_{lock})$ during the first measurement of the pulse rising edge is maximized. For a direct comparison with experimental data taken (Fig. 1 Left), V_{err} is shown in Fig. 2 (Right) for the three algorithms using a slew rate very close to the unlock point of the PI controller. While the PI controller becomes trapped in the nonlinear regime as in the experimental measurement, PC1 and PC2 both recover from the nonlinear regime within three or four frames. The readout error of the flux measurement $(\Phi_{in} - \Phi_{measured})$ for the PI controller and PC2 are shown in Fig. 3. The PI controller unlocks at $\mathrm{d}\Phi_{in,0}/\mathrm{d}t = 0.243\ \Phi_0$/frame, PC1 unlocks at $\mathrm{d}\Phi_{in,0}/\mathrm{d}t = 0.270\ \Phi_0$/frame, and PC2 unlocks at $\mathrm{d}\Phi_{in,0}/\mathrm{d}t = 0.328\ \Phi_0$/frame. Since pulse arrival time is random, these unlock points indicate the maximum slew rate for which the controllers can track all non-pileup events. Thus, while retaining all events, PC2 has a 35% advantage in maximum slew rate over the PI controller.

The predictive controllers have an even larger advantage over the PI controller if the measurement application allows imperfect retention of high-slew rate events. As shown in Fig. 4, the unlocking behaviors of PC1 and PC2 are strongly dependent on pulse arrival time. PC2 can track a pulse with $\mathrm{d}\Phi_{in,0}/\mathrm{d}t = 0.480\ \Phi_0$/frame if the pulse has optimal arrival time, an 81% advantage in optimal pulse arrival time $\mathrm{d}\Phi_{in,0}/\mathrm{d}t|_{max}$ over the PI controller.

4 Conclusion

Our simulations find that a predictive control algorithm could increase TDM's maximum TES current slew rate by 35% without reducing event retention rates. Using commonly employed TDM scaling techniques, this algorithm would scale maximum

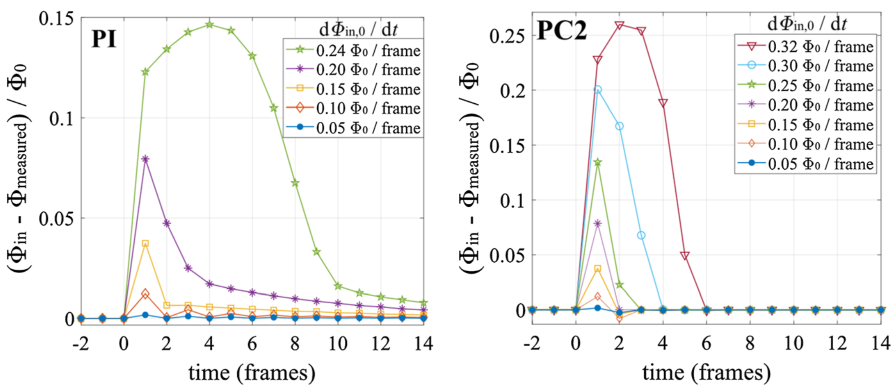

Fig. 3 Simulated SQ1 flux measurement error with zero phase offset pulses for the PI controller (Left) and PC2 (Right). $\mathrm{d}\Phi_{in,0}/\mathrm{d}t$ for each pulse is listed in the legend (Color figure online)

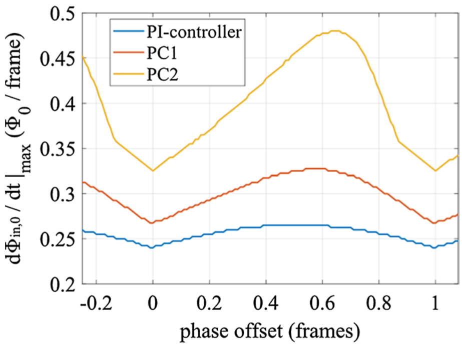

Fig. 4 Each algorithm's maximum $d\Phi_{in,0}/dt$ before unlocking ($d\Phi_{in,0}/dt|_{max}$) is plotted against pulse phase offset, given by pulse arrival time minus sampling time. Performance at V_{err0} other than 50% can be estimated by applying a factor of (100%−V_{err0})/50% adjustment to $d\Phi_{in,0}/dt|_{max}$ (Color figure online)

row count by a factor of $(1.35)^{2/3}$ [15] while keeping readout noise constant. Thus, 40-row TDM [6] would scale to 48-row TDM for X-IFU, lowering the 50 mK multiplexer power output by a factor of 0.83 per TES. Additionally, the predictive controller would allow the measurement of X-ray events with far greater energies than the 12 keV specified for X-IFU with imperfect event retention. Future work will include implementing the predictive controller in firmware so that this concept can be tested with real devices.

Acknowledgements This work was supported by the NASA SAT program, "Providing Enabling & Enhancing Technologies for a Demonstration Model of the Athena X-IFU." The authors thank collaborators at NASA, Stanford, NIST, and CNES for their helpful technical discussions.

References

1. W.B. Doriese et al., Rev. Sci. Instrum. **88**, 053108 (2017). https://doi.org/10.1063/1.4983316
2. G.C. O'Neil et al., J. Low Temp. Phys. (This Special Issue) (2019)
3. S. Yamada et al., J. Low Temp. Phys. (This Special Issue) (2019)
4. H. Tatsuno et al., J. Low Temp. Phys. (This Special Issue) (2019)
5. W.B. Doriese et al., IEEE Trans. Appl. Supercond. **29**, 2500305 (2019). https://doi.org/10.1109/TASC.2019.2905577
6. M. Durkin et al., IEEE Trans. Appl. Supercond. **29**, 2101005 (2019). https://doi.org/10.1109/TASC.2019.2904472
7. D. Barrett et al., Proc. SPIE **9905**, 99052F (2016). https://doi.org/10.1117/12.2232432
8. W.B. Doriese et al., Correlation between Fe-V-C alloys surface hardness and plasma temperature via LIBS technique. J. Low Temp. Phys. **184**, 389–229 (2016). https://doi.org/10.1007/s10909-015-1373-z
9. C.D. Reintsema et al., Rev. Sci. Instrum. **74**, 4500 (2003). https://doi.org/10.1063/1.1605259
10. K.M. Morgan et al., Appl. Phys Lett. **109**, 112604 (2016). https://doi.org/10.1063/1.4962636
11. S.J. Smith et al., J. Low Temp. Phys. (This Special Issue) (2019)
12. A. Miniussi et al., Analysis of copper surface features obtained using TEA CO 2 laser at reduced air pressure. Appl Surf Sci **193**, 337 (2018). https://doi.org/10.1016/j.apsusc.2013.01.067
13. J.W. Fowler et al., J. Low Temp. Phys. **184**, 374 (2016). https://doi.org/10.1007/s10909-015-1380-0
14. S. Bibian, H. Jin, IEEE Trans. Power Electr. **15**, 835 (2000)
15. W.B. Doriese et al., J. Low Temp. Phys. **167**, 595 (2012). https://doi.org/10.1007/s10909-012-0509-7